

FUMES. II. Ly α Reconstructions of Young, Active M DwarfsALLISON YOUNGBLOOD,^{1,2} J. SEBASTIAN PINEDA,¹ AND KEVIN FRANCE^{1,3,4}¹*Laboratory for Atmospheric and Space Physics, University of Colorado, 600 UCB, Boulder, CO 80309, USA*²*NASA Goddard Space Flight Center, Greenbelt, MD 20771, USA*³*Department of Astrophysical and Planetary Sciences, University of Colorado, UCB 389, Boulder, CO 80309, USA*⁴*Center for Astrophysics and Space Astronomy, University of Colorado, 389 UCB, Boulder, CO 80309, USA*

ABSTRACT

The H I Ly α (1215.67 Å) emission line dominates the far-UV spectra of M dwarf stars, but strong absorption from neutral hydrogen in the interstellar medium makes observing Ly α challenging even for the closest stars. As part of the Far-Ultraviolet M-dwarf Evolution Survey (FUMES), the *Hubble Space Telescope* has observed 10 early-to-mid M dwarfs with ages ranging from ~ 24 Myr to several Gyrs to evaluate how the incident UV radiation evolves through the lifetime of exoplanetary systems. We reconstruct the intrinsic Ly α profiles from STIS G140L and E140M spectra and achieve reconstructed fluxes with 1- σ uncertainties ranging from 5% to a factor of two for the low resolution spectra (G140L) and 3-20% for the high resolution spectra (E140M). We observe broad, 500-1000 km s⁻¹ wings of the Ly α line profile, and analyze how the line width depends on stellar properties. We find that stellar effective temperature and surface gravity are the dominant factors influencing the line width with little impact from the star's magnetic activity level, and that the surface flux density of the Ly α wings may be used to estimate the chromospheric electron density. The Ly α reconstructions on the G140L spectra are the first attempted on $\lambda/\Delta\lambda \sim 1000$ data. We find that the reconstruction precision is not correlated with SNR of the observation, rather, it depends on the intrinsic broadness of the stellar Ly α line. Young, low-gravity stars have the broadest lines and therefore provide more information at low spectral resolution to the fit to break degeneracies among model parameters.

Keywords: M dwarf stars, stellar atmospheres, interstellar absorption, planet-hosting stars

1. INTRODUCTION

Far-ultraviolet (FUV) photons (912-1700 Å) drive photochemistry and heating in planetary upper atmospheres due to the large, wavelength-dependent absorption cross sections of molecules throughout the FUV (e.g., Segura et al. 2005; Loyd et al. 2016). Using the *Hubble Space Telescope* (HST), the Far-Ultraviolet M-dwarf Evolution Survey (FUMES; HST-GO-14640) has measured the FUV spectral energy distributions of early-to-mid M dwarfs ranging in age from 24 Myr to field age (~ 5

Gyr) to determine how stellar magnetic activity evolves with age and to better inform exoplanet atmosphere evolution studies (Pineda et al. *accepted*). In particular, a large ratio of incident FUV to near-ultraviolet (NUV; 1700–3200 Å) flux on a planet can lead to the abiotic production of oxygen and ozone, possible biosignatures (see reviews by Meadows et al. 2018 and Schwieterman et al. 2018). M dwarfs have intrinsically faint FUV and NUV emission from their cool photospheres, but high levels of magnetic heating (e.g., non-radiative heating) make bright chromospheric and transition region emission lines that raise the FUV/NUV flux ratio two to three orders of magnitude higher than for solar-type stars.

H I Ly α (1215.67 Å) is the brightest M dwarf emission line in the UV (France et al. 2013), and is therefore required for a thorough accounting of the stellar UV energy budget. Yet, neutral hydrogen gas in the ISM completely attenuates the inner ~ 80 – 100 km s $^{-1}$ of the Ly α line core for even the closest stars. To determine the intrinsic stellar emission, the Ly α line must be reconstructed from the observed wings. Historically, this has been done at high spectral resolving power ($\lambda/\Delta\lambda > 40,000$) so that the D I absorption line (-82 km s $^{-1}$ from H I) can be resolved from the H I absorption line (e.g., Wood et al. 2005). Resolving the optically thin D I line places strong constraints on the properties of the highly optically thick H I line: column density, radial velocity, and Doppler broadening. France et al. (2013) showed that reliable reconstructions can be performed at lower resolving power ($\lambda/\Delta\lambda \sim 10,000$). For the first time, we present reconstructions at an even lower spectral resolving power ($\lambda/\Delta\lambda \sim 1,000$), where the H I absorption trough is completely unresolved.

The higher sensitivity of the G140L spectra compared to higher resolution STIS gratings (G140M, E140M, and E140H) eases the detection of the important Ly α line, expanding the volume of M dwarfs for which Ly α emission can potentially be studied. Higher sensitivity also allows for the measurement of very broad Ly α wings (~ 500 – 1000 km s $^{-1}$), which have been long known for the Sun (Morton & Widing 1961) and for M dwarfs (Gayley 1994; Youngblood et al. 2016). The broad wings are the result of partial frequency redistribution, which occurs because Ly α is a highly optically thick resonance line (Milkey & Mihalas 1973; Basri et al. 1979). Photons from the lower opacity lower transition region escape in the line core, whereas photons from the higher opacity chromosphere must diffuse out into the broad wings to escape. Matching the observed wing strength of emission lines like Ly α is a notoriously difficult problem for stellar models, especially for M dwarf models (see Fontenla et al. 2016; Peacock et al. 2019a; Tilipman et al. 2020). More detailed observational constraints support the upcoming generation of stellar models that include chromospheres and transition regions (Peacock et al. 2019b; Tilipman et al. 2020).

The intensity of the chromospheric emission line wings compared to the line core is controlled primarily by the pressure scale height (Ayres 1979), with an inverse dependence on surface gravity. For main sequence stars, this means that more massive stars have brighter wings, as shown by Wilson & Bappu (1957) for Ca II H&K. However, there is likely a small dependence on magnetic activity (Ayres 1979; Gayley 1994), with more active stars exhibiting stronger wings. Combining the young, active M dwarf sample of FUMES, two well-known active M dwarfs from the literature (Proxima Centauri and AU Mic), and the more inactive M dwarf sample from the MUSCLES Treasury Survey (France et al. 2016; Youngblood et al. 2016; Loyd et al. 2016), we address the magnitude of magnetic activity’s effect on the observed Ly α wing strength of M dwarf stars.

In Section 2, we briefly describe the FUMES observations and reductions, and in Section 3 we thoroughly describe the Ly α reconstructions. These results are used in the main FUMES analysis

Table 1. FUMES Targets

Name	Other Name	Spectral Type	d (pc)	P_{rot} (d)	M (M_{\odot})	R (R_{\odot})	T_{eff} (K)	Age	STIS grating
G 249-11		M4	29.14	52.8 ^a	0.24	0.26	3277	field ^e	G140L
HIP 112312	WW PsA	M4.5	20.86	2.4 ^b	0.25	0.69	3173	24 Myr ^f	E140M
GJ 4334	FZ And	M5	25.33	23.5 ^a	0.29	0.31	3260	field ^g	G140L
LP 55-41		M3	37.04	53.4 ^a	0.41	0.42	3412	field ^e	G140L
HIP 17695		M4	16.8	3.9 ^b	0.44	0.50	3393	150 Myr ^f	E140M
LP 247-13		M3.5	35.04	1.3 ^c	0.50	0.49	3511	650 Myr ^h	G140L
GJ 49		M1	9.86	18.6 ^d	0.54	0.53	3713	field ⁱ	G140L
GJ 410	DS Leo	M0	11.94	14.0 ^d	0.56	0.55	3786	300 Myr ^h	G140L
CD -35 2722		M1	22.4	1.7 ^b	0.57	0.56	3727	150 Myr ^f	G140L
HIP 23309		M0	26.9	8.6 ^b	0.79	0.93	3886	24 Myr ^f	G140L

NOTE—Distances (d) from Gaia Data Release 2 (Brown et al. 2018); spectral types, effective temperatures (T_{eff}), masses (M), and radii (R) from Pineda et al. *accepted*.

References—(a) Donati et al. (2008), (b) Hartman et al. (2011), (c) Messina et al. (2010), (d) Newton et al. (2016), (e) Gagné & Faherty (2018), (f) Bell et al. (2015), (g) Irwin et al. (2011), (h) Shkolnik & Barman (2014), (i) Miles & Shkolnik (2017).

(Pineda et al. *accepted*). In Section 4, we analyze the broad Ly α wings and the implications for understanding M dwarf atmospheres. In Section 5, we summarize our findings.

2. OBSERVATIONS AND REDUCTIONS

Using the STIS spectrograph onboard *HST*, we observed 10 M dwarfs as part of the The Far-Ultraviolet M-dwarf Evolution Survey (FUMES) survey (GO 14640; PI: J. S. Pineda). Properties of the targets are listed in Table 1 and discussed in more detail in Paper I (Pineda et al. *accepted*). Two of the targets, LP 55-41 and G 249-11, were detected at low signal-to-noise ratio (SNR), and we do not attempt Ly α reconstructions for them. Custom reductions were performed using `stistools`¹ following Loyd et al. (2016), including the exclusion of flares from the extracted spectra of GJ 4334, GJ 410, and HIP 17695. See Pineda et al. (*under review*) for more details.

3. Ly α RECONSTRUCTIONS

3.1. The Model

Our model is comprised of two components: the stellar emission component and the ISM absorption component. We tested different functions for the intrinsic stellar emission, including multiple, superimposed Gaussians, and found that a single Voigt profile in emission fits both the line core and the broad wings best. We use the `astropy Voigt1D` function, which is based on the computation from McLean et al. (1994). We assume no self-reversal because past results have shown that

¹ <https://stistools.readthedocs.io/en/latest/>

the Ly α self-reversal of M dwarfs is small (Wood et al. 2005; Guinan et al. 2016), if present at all (Youngblood et al. 2016; Bourrier et al. 2017; Schneider et al. 2019). Given that the Ly α line center, the region in the spectrum where the self-reversal appears, is usually entirely hidden by the ISM and not well-constrained by the reconstruction, we assume no self-reversal is present. The Voigt emission line model component has four free parameters:

$$F_{\text{emission}}^{\lambda} = \mathcal{V}(\lambda, V_{\text{radial}}, A, FWHM_L, FWHM_G), \quad (1)$$

where V_{radial} is the radial velocity of the emission line (km s^{-1}), A is the Lorentzian amplitude ($\text{erg cm}^{-2} \text{s}^{-1} \text{\AA}^{-1}$; note that we parameterize it in all tables as $\log_{10} A$), and $FWHM_L$ and $FWHM_G$ (km s^{-1}) are the full-width at half maximum values for the Lorentzian and Gaussian components, respectively. For use with `Voigt1D`, V_{radial} , $FWHM_L$, and $FWHM_G$ are converted to \AA . For the reconstructions on the E140M spectra where Ly α and Si III are not blended, Equation 1 is used, but for the G140L spectra where the two lines are blended, $F_{\text{emission}}^{\lambda} = F_{\text{emission,HI}}^{\lambda} + F_{\text{emission,SiIII}}^{\lambda}$.

We assume a single ISM absorbing cloud as such low-resolution spectra (300 km s^{-1}) are not able to distinguish between $\sim 20\text{--}40 \text{ km s}^{-1}$ separated clouds. Youngblood et al. (2016) demonstrated that assuming a single-velocity ISM does not significantly impact the reconstructed Ly α flux. For the ISM component (used for Ly α only), we model the H I and D I absorption lines each as Voigt profiles with linked parameters using the code `lyapy`² (Youngblood et al. 2016):

$$F_{\text{absorption}}^{\lambda} = \mathcal{V}(\lambda, V_{HI}, \log_{10} N(HI), b_{HI}) \times \mathcal{V}(\lambda, V_{DI}, \log_{10} N(DI), b_{DI}). \quad (2)$$

V_{HI} is the radial velocity (km s^{-1}) and is assumed to be the same for both H I (1215.67 \AA) and D I (1215.34 \AA) ($V_{HI} = V_{DI}$, so V_{HI} is the reported parameter). $\log_{10} N$ is the logarithm of the column density (cm^{-2}) where $N(HI)$ and $N(DI)$ are linked by the parameter D/H, the deuterium to hydrogen ratio: $N(DI) = N(HI) \times D/H$. D/H is fixed to 1.5×10^{-5} (Linsky et al. 2006), so $\log_{10} N(HI)$ is the reported parameter. The Doppler parameter b controls the width of the absorption line, and we link b_{HI} and b_{DI} so that $b_{DI} = b_{HI}/\sqrt{2}$. b_{HI} is the reported parameter. In order to reduce the number of free parameters for the G140L reconstructions, b_{HI} was fixed at 11.5 km s^{-1} based on the standard $T=8000 \text{ K}$ ISM (Wood et al. 2004; Redfield & Linsky 2004).

To model the observed (attenuated) profile, we multiply the emission and absorption models (Equations 1 & 2) and convolve with the instrument line spread function (LSF) provided by STScI³ for the appropriate grating and slit combinations to recover the true physical parameters and account for the non-Gaussian wings of the G140L LSF:

$$F^{\lambda} = (\mathcal{V}_{\text{emission}} \times \mathcal{V}_{\text{absorption}}) \otimes LSF. \quad (3)$$

3.2. Fitting procedure and results

To reconstruct the Ly α profiles, we used a likelihood-based Bayesian calculation and a Markov-Chain Monte Carlo (MCMC) method (`emcee`⁴; Foreman-Mackey et al. 2013) to simultaneously fit the model (Equation 3) to the observed spectra. We assume uniform (flat) priors for all parameters

² <https://github.com/allisony/lyapy>

³ <https://www.stsci.edu/hst/instrumentation/stis/performance/spectral-resolution>

⁴ <https://emcee.readthedocs.io/en/latest/>

except for a logarithmic prior for the Doppler b value (Youngblood et al. 2016), and a Gaussian likelihood

$$\ln \mathcal{L} = -\frac{1}{2} \sum_i^N \frac{(y_i - y_{model,i})^2}{\sigma_{y_i}^2} + \ln(2\pi\sigma_{y_i}^2), \quad (4)$$

where N is the total number of spectral data points y_i with associated uncertainties σ_{y_i} , and $y_{model,i}$ corresponds to Equation 3. We maximize the addition of $\ln \mathcal{L}$ and the logarithm of our priors with `emcee`. We used 50 walkers, ran for 50 autocorrelation times ($\sim 10^5$ - 10^6 steps), and removed an appropriate burn-in period based on the behavior of the walkers.

Tables 3-7 show all of our model parameters with the assumed priors (uniform or logarithmic) within a bounded range and the 2.5, 15.9, 50, 84.1, and 97.5 percentiles as determined from the marginalized posterior distributions. We present the median (50th percentile) as the best fit parameter values. The best fit (median) and 68% and 95% confidence intervals on the reconstructed $\text{Ly}\alpha$ and Si III fluxes were determined from the entire ensemble (i.e., a histogram of all the $\text{Ly}\alpha$ or Si III fluxes from the MCMC chain). Often the median parameter values do not create a self consistent solution, so we obtain the best fit models and reconstructed profiles from the median flux in each wavelength bin from the ensemble of models and reconstructed profiles. Figure 1 shows the best fit model and reconstructed profile for the HIP 23309 data, and Figure 2 shows the marginalized and joint probability distributions of the fitted parameters for HIP 23309. Similar figures for the other stars are available in the figure set in the online journal.

In the rest of this section, we make note of any irregularities or the source of any constraints imposed on the reconstructions on a star-by-star basis. Most of the FUMES $\text{Ly}\alpha$ spectra were obtained with the low-resolution G140L STIS grating ($\lambda/\Delta\lambda \sim 1000$), where the H I and D I ISM absorption lines are unresolved. Resolving the D I absorption is useful for constraining the ISM model parameters (column density, Doppler b value, and radial velocity), so we provide constraints on these parameter values with outside information when necessary to aid convergence to a best-fit solution. These constraints include stellar radial velocities from SIMBAD, predicted ISM radial velocities from the Local ISM Kinematic Calculator⁵ (Redfield & Linsky 2008), predicted H I column densities for the local interstellar cloud (LIC)⁶ (Redfield & Linsky 2000), and measured H I column densities from nearby sightlines collated from Wood et al. (2005), Youngblood et al. (2016), and Youngblood et al. (2017).

GJ 4334—The fit had to be restricted to $\log_{10} N(\text{HI}) > 17.8$, because the fit preferred a $\log_{10} N(\text{HI}) < 17.8$ solution. The likelihood values are not higher at $\log_{10} N(\text{HI}) < 17.8$, but the parameter space is much more well-behaved (i.e., smoothly varying), which is likely why the fit prefers this parameter regime. With $\log_{10} N(\text{HI})$ restricted to lie between 17.8-19, the best fit $\log_{10} N(\text{HI}) = 18.03$ is in agreement with the LIC model $\log_{10} N(\text{HI}) = 18.04$ prediction and measurements of nearby sightlines ($\log_{10} N(\text{HI})=17.9$ -18.5).

HIP 17695—Despite the high spectral resolution obtained for this target, the fit is not consistent with probable $\log_{10} N(\text{HI})$ values (>17.5). The MCMC prefers the $\log_{10} N(\text{HI})$ value low (<17.0),

⁵ <http://lism.wesleyan.edu/LISMdynamics.html>

⁶ <http://lism.wesleyan.edu/ColoradoLIC.html>

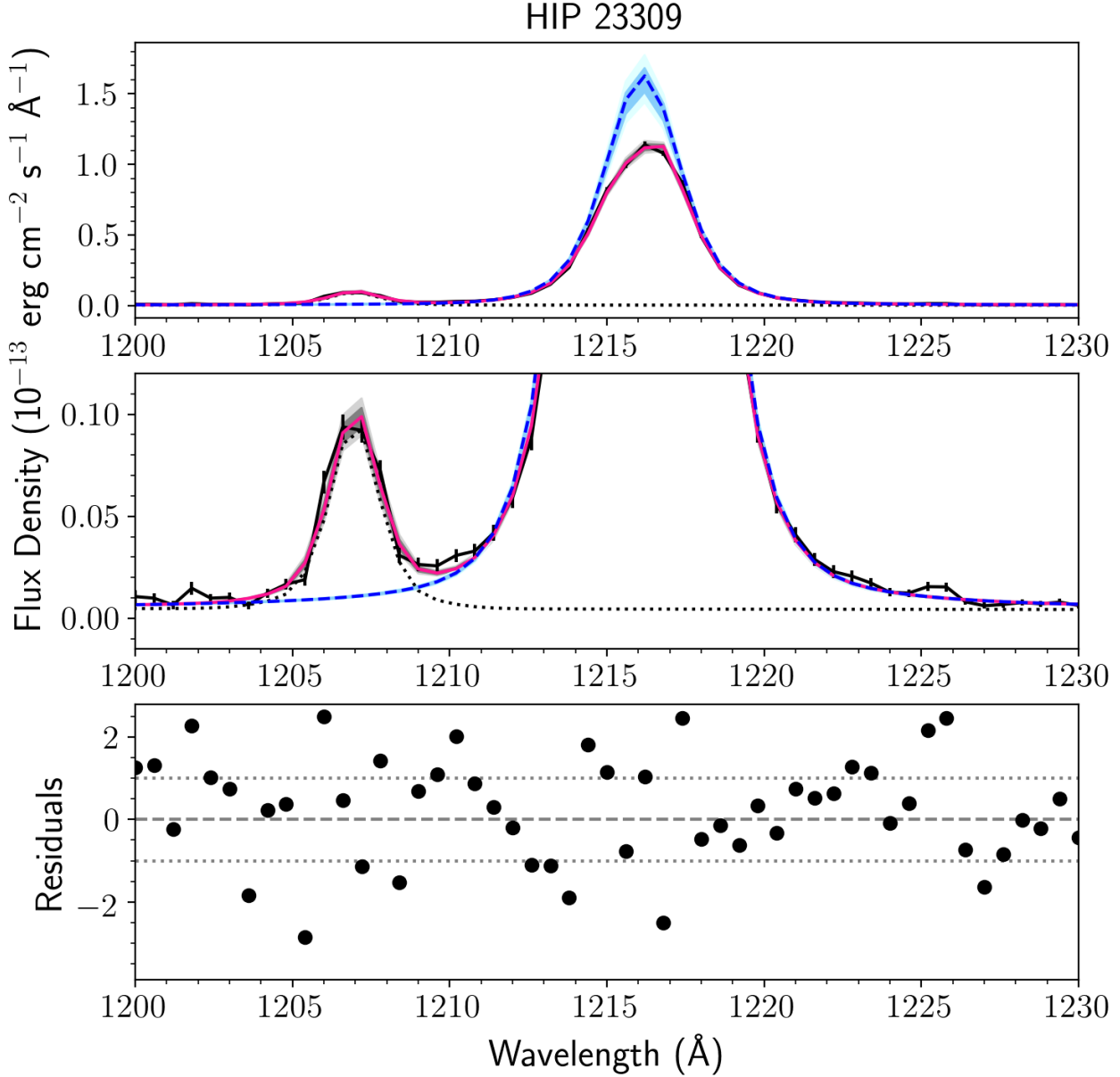


Figure 1. HIP 23309 best fit Ly α reconstruction. In the upper two panels, the STIS data with $1\text{-}\sigma$ error bars are shown in black, the best model fit (intrinsic Ly α profile folded through the ISM) is shown in pink with 1σ error bars shown in dark shaded gray and 2σ error bars in light shaded gray. The dashed blue line shows the best fit intrinsic Ly α profile with 1- and $2\text{-}\sigma$ error bars (dark and light shaded blue, respectively), and the dotted black line shows the Si III best fit profile. The bottom panel shows the residuals ((data-model)/(data uncertainty)) for the best fit model (pink in the upper panels) that best fits the data (black in the upper panels). The horizontal dashed line is centered at zero, and the dotted lines are centered at ± 1 .

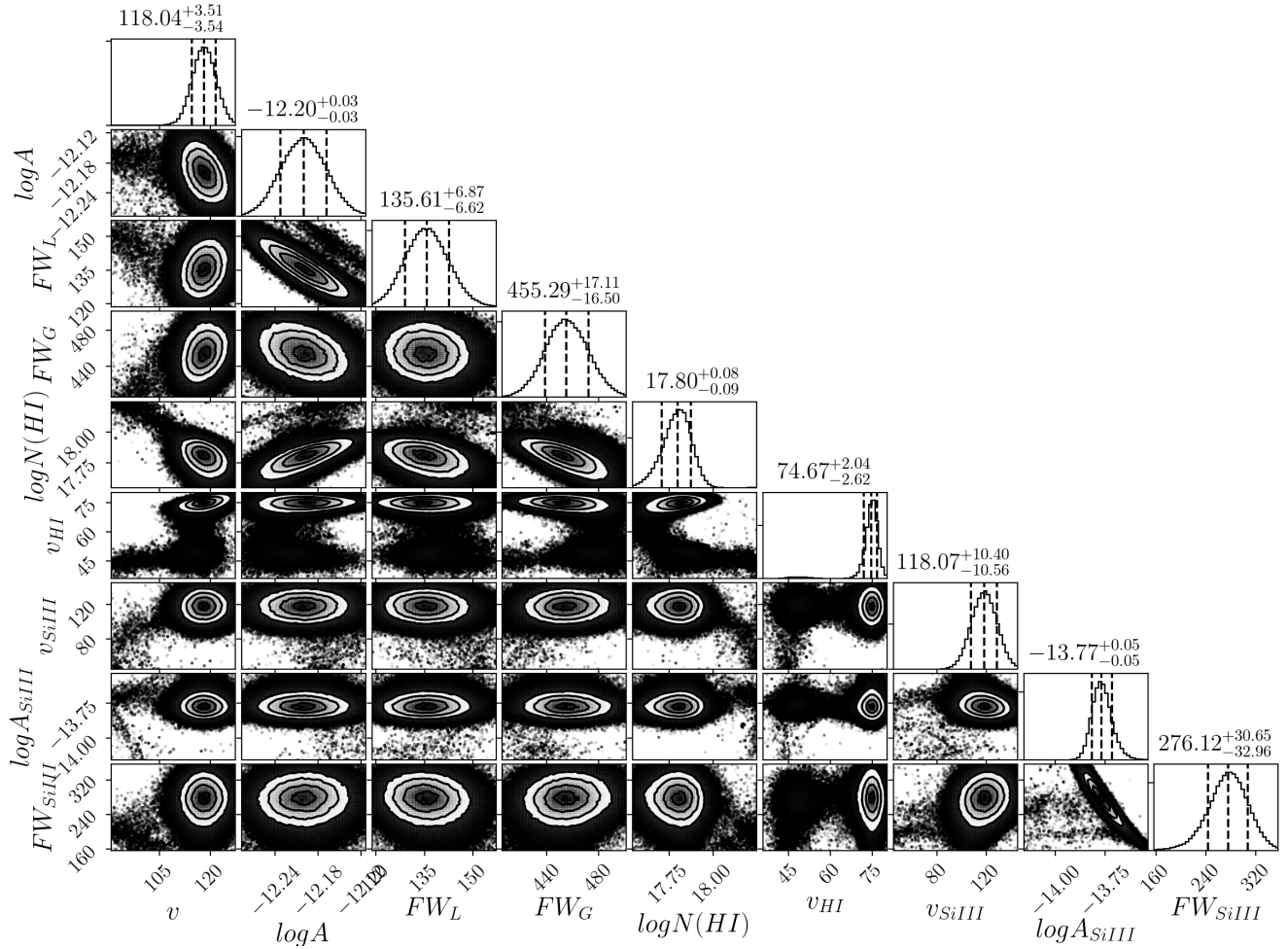


Figure 2. One- and two-dimensional projections of the sampled posterior probability distributions, referred to as marginalized and joint distributions, respectively, of the nine parameters for HIP 23309. Contours in the joint distributions are shown at 0.5-, 1-, 1.5-, and 2- σ , and the histograms’ dashed black vertical lines show the 16th, 50th, and 84th percentiles of the samples in each marginalized distribution. The text above each histogram shows the median \pm the 68% confidence interval.

which may be unphysically low based on knowledge of the local ISM (Wood et al. 2005), although a value <18.0 is justified based on literature measurements of nearby sightlines. We constrain the column density to be between 17.8-18.0, in agreement with the LIC model’s predictions $\log_{10} N(\text{HI}) = 17.93$, and allow the MCMC to pile up near the lower boundary. We note that O V (1218.3 Å) is clearly detected in the Ly α red wing.

LP 247-13—We constrain the $\log_{10} N(\text{HI})$ parameter to be between 18.3-19.0 (the fit prefers <18.0) based on a previous measurement of $\log_{10} N(\text{HI}) = 18.31$ for a foreground star (Dring et al. 1997).

GJ 49—The fit reveals 4 different local maxima with no clear global maximum. We discard the solutions with a low $\log_{10} N(\text{HI}) = 17.7$ value and a high $\log_{10} N(\text{HI}) = 18.7$ value, because nearby sightlines indicate $\log_{10} N(\text{HI}) = 18.0$ -18.3. We also rule out the solution with the $>100 \text{ km s}^{-1}$ dif-

ference between V_{HI} and V_{radial} . With these restrictions on $N(HI)$ and V_{HI} in place (see priors in Table 3), we ran the MCMC for the presented solution.

GJ 410—The posterior distribution for this star’s fit is wide, as the 95% confidence interval spans a factor of 15 in $Ly\alpha$ flux. Nearby sightlines indicate $\log_{10} N(HI)$ lies in the range of 17.6–18.6, and the solution’s $\log_{10} N(HI) = 18.32$ is in agreement with this range.

3.3. Analysis of the reconstruction quality

The quality of the E140M reconstructions is high, but for many of our G140L reconstructions, >32% of the residuals lie outside of the $\pm 1\text{-}\sigma$ range (Figure 1 and the extended figure set in the online journal). This indicates either that the data uncertainties are underestimated or that the model is misspecified. In general, the data appear well-fit by the model, but a Durbin-Watson test (Durbin & Watson 1950) reveals some positive autocorrelation in the residuals. For half of our stars (HIP 23309, GJ 410, LP 247-13, HIP 112312), the Durbin-Watson statistic (dw) is between 1.5–1.8 (where 2 represents no autocorrelation and 0 represents perfect positive autocorrelation) and for the others (GJ 49, CD -35 2722, GJ 4334, HIP 17695) $dw = 1.1$ –1.4. This autocorrelation of the residuals can be partially accounted for by a group of weak, unresolved emission lines present around 1190–1210 Å that are not included in our model. Based on detailed spectra of the Sun (Curd et al. 2001) and prominent lines in high quality M dwarf spectra like AU Mic (Pagano et al. 2000; Ayres 2010) and GJ 436 (dos Santos et al. 2019), these lines include S III (1190, 1194, 1201, 1202 Å), Si II (1190, 1193, 1194, 1197 Å), N I (1200, 1201 Å), Si III (1206 Å), and H₂ (1209 Å)⁷. There are fewer unresolved emission lines in the blue wing of the $Ly\alpha$ line, including O V (1218 Å) and S I (1224, 1229, 1230 Å). This creates an apparent asymmetry (see the solar spectrum from Woods et al. 1995), whereas our model is symmetric about the line center. We have included only the strongest of these adjacent emission lines (Si III at 1206 Å) in our model as the others are ill-constrained by our spectra.

We have tested adding a scatter term (f) to our model to account for underestimated data uncertainties, which is implemented by replacing the σ_i^2 terms in Equation 4 with $\sigma_i^2 + f^2$. We find that for our higher quality fits (e.g., HIP 23309), the fitted result was the same. For our lowest quality fit (GJ 49), there was a large difference in the reconstructed flux, but the quality of the fit was not improved as the structure in the residuals remained. Therefore, we do not present the fits with the scatter term in this work. We conclude that the model is missing a component, such as the weak emission lines and/or continua in the line wings mentioned above.

GJ 49’s reconstruction quality is the worst of our sample; and we note that its reconstructed $Ly\alpha$ flux should be interpreted with caution. We postulate that the reason this star’s fit is so unconstrained is because of its $Ly\alpha$ line’s narrow intrinsic width (see Section 4.3) and the high SNR of its spectrum. GJ 49’s observed spectrum has higher SNR around the $Ly\alpha$ line than any of our other G140L spectra, and this precision increases the visibility of features not covered by our model. Other FUMES targets with wider intrinsic line widths (and lower SNR) may swamp the signals from unresolved emission lines and/or continua. Despite large scatter in the residuals, GJ 49’s $Ly\alpha$ and Si III flux measurements appear to be consistent with other FUMES targets of similar rotation period (Pineda et al. *accepted*).

⁷ Note that in dos Santos et al. (2019), this line is labeled as Si IV, but is most likely H₂ as labeled in the SUMER solar spectral atlas (Curd et al. 2001).

Regarding our fitted radial velocity parameters, we note that the relative accuracy of the STIS MAMA’s wavelength solution is reported in the STIS Instrument Handbook as 0.25-0.5 pixels (37-74 km s^{-1} for the G140L grating; 0.8-1.6 km s^{-1} for the E140M grating), and the absolute wavelength accuracy is 0.5-1 pixel (74-148 km s^{-1} for G140L; 1.6-3.3 km s^{-1} for E140M). We find that the quoted relative wavelength accuracy can easily describe the offsets between our fitted H I and Si III radial velocities (accounting for the 68% confidence interval on those values). The quoted absolute wavelength accuracy can account for almost all of the offsets between the literature stellar radial velocities and our fitted radial velocities. The exception is GJ 4334, which has some disagreement in the literature over its radial velocity ($-40 \pm 4 \text{ km s}^{-1}$ from [Newton et al. 2014](#); $-16.5 \pm 4.0 \text{ km s}^{-1}$ from [Terrien et al. 2015](#); -11.9 km s^{-1} from [West et al. 2015](#)). This discrepancy is not large enough to account for the $\sim 200\text{-}300 \text{ km s}^{-1}$ offset between our fitted radial velocities and the literature values. However, GJ 4334’s velocity difference between the fitted radial velocity and the fitted ISM radial velocity is in agreement with the velocity difference of the [Newton et al. \(2014\)](#) radial velocity and predicted ISM velocity ($6.0 \pm 1.4 \text{ km s}^{-1}$; [Redfield & Linsky 2008](#)), lending confidence to our fit and supporting the possibility that the absolute wavelength accuracy for GJ 4334’s STIS observation is poorer than is typical.

To test the accuracy of the reconstructions based on the G140L spectra, we degraded the resolution of our E140M spectra (HIP 112312 and HIP 17695) to the resolution of the G140L spectra by convolving with the G140L LSF and rebinning to match the G140L dispersion. Tables 6-7 show the results of the E140M (native resolution) and degraded resolution reconstructions for these two stars. There is substantial overlap between the native and degraded reconstructed $\text{Ly}\alpha$ fluxes at the 68% (for HIP 17695) and the 95% confidence interval (for both). The uncertainties with the G140L-quality reconstruction are much larger than for the E140M reconstructions, as expected. When comparing the individual fitted parameter values, we find that the G140L-quality reconstructions do not always agree with their higher resolution counterparts. For HIP 17695, agreement between the individual fitted parameters is generally good, but not for HIP 112312. We provide confidence intervals for all of our G140L reconstruction parameters (Tables 3-5), but note that they should be interpreted with caution and may not reflect the true parameters that could be revealed with higher-resolution spectra. This may be because the G140L posterior distributions are generally very wide, and we report the median parameter values as the best-fit values, even though combining the median parameter values does not always yield a self-consistent best-fit to the data. However, this exercise in comparing E140M reconstructions with degraded resolution reconstructions shows that the reconstructed $\text{Ly}\alpha$ fluxes overlap within at least the 95% level.

4. DISCUSSION

4.1. *The Wilson-Bappu effect and $\text{Ly}\alpha$ line widths*

Our STIS G140L reconstructed spectra of M dwarfs show their broad, $\sim 500\text{-}1000 \text{ km s}^{-1}$ $\text{Ly}\alpha$ wings in detail (Figure 3). As demonstrated in [Ayres \(1979\)](#), the widths of chromospheric emission lines like Ca II H&K, Mg II h&k, and $\text{Ly}\alpha$ are predominantly controlled by the stellar temperature distribution rather than chromosphere dynamics or magnetic heating. This explains the remarkable Wilson-Bappu correlation between absolute stellar magnitude and FWHM for the Ca II H&K emission cores ([Wilson & Bappu 1957](#)) and other chromospheric emission lines ([McClintock et al. 1975](#); [Cassatella et al. 2001](#)) across many orders of magnitude of stellar bolometric luminosity. In Figure 4, we show

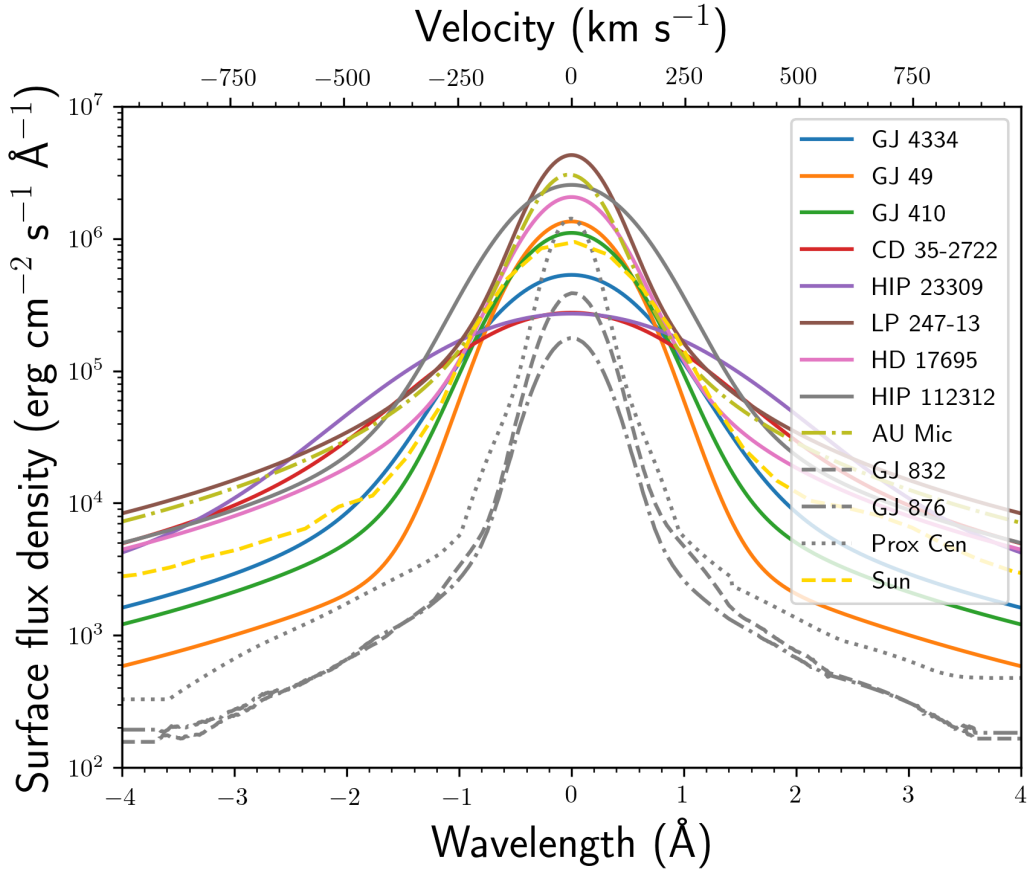


Figure 3. Reconstructed Ly α profiles (corrected for stellar distance and radius) with the effect of instrumental broadening removed (with the exception of the Sun, whose line profile inside ± 2 Å is dominated by instrumental broadening) are shown for the FUMES sample and several comparison stars in dashed/dotted lines including the Sun (McClintock et al. 2005), AU Mic, Proxima Centauri, GJ 832, and GJ 876 (Youngblood et al. 2016). The profiles have been shifted in wavelength to set the peak emission at 0 km s $^{-1}$.

that our data support a similar correlation ($\rho=0.72$; $p=0.0015$) between bolometric luminosity and Ly α FWHM, albeit over a much smaller parameter space than explored by Wilson & Bappu (1957).

Ayres (1979) notes that stellar magnetic activity (e.g., due to non-radiative heating) does play a role in the widths of chromosphere emission lines, with greater activity corresponding to wider lines, in addition to the stronger influences of stellar effective temperature, surface gravity, and elemental abundance compared to hydrogen. Ayres (1979) and Linsky (1980) present a linear model of chromospheric emission line width as a function of chromospheric heating (i.e., activity as measured by the flux of a chromospheric emission line), effective temperature, surface gravity, and elemental abundance. To determine which stellar properties are most responsible for our observed Ly α widths, we construct a linear model based on our observations. We select surface gravity, Si III luminosity as a fraction of bolometric luminosity (a general “activity” proxy), and effective temperature as predictor variables. Because we are examining a hydrogen line, we do not include a metallicity term. We scale each variable (by subtracting the mean and dividing by the standard deviation), construct a correlation matrix, and calculate the eigenvalues and eigenvectors via principal component analysis (PCA) (Table 4). Only the first two principal components (PCs) or eigenvectors have eigenvalues

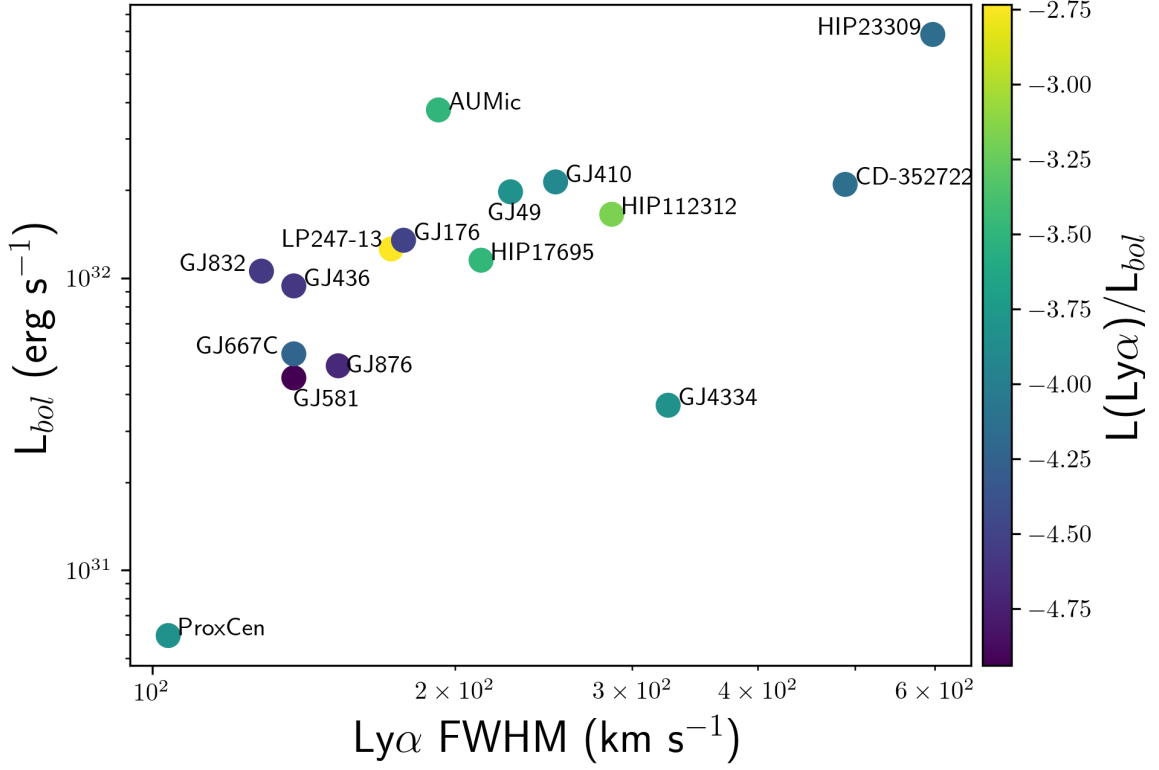


Figure 4. Intrinsic $\text{Ly}\alpha$ FWHM (km s^{-1}) versus stellar bolometric luminosity, plotted analogously to Wilson & Bappu (1957), and color coded by $\text{Ly}\alpha$ luminosity as a fraction of bolometric luminosity. The effect of instrument line broadening has been removed. The Pearson correlation coefficient ($\rho=0.72$, $p=0.0015$) demonstrates a statistically significant correlation over this narrow range of parameter space.

>1 or are correlated significantly ($|\rho| > 0.5$; $p < 0.05$) with any of the predictor variables; therefore, we only include PC_1 and PC_2 in the linear model of $\text{Ly}\alpha$ width.

We perform a multiple linear regression to relate our previously determined PCs to a response variable, the $\text{Ly}\alpha$ full width at 20% maximum flux ($\text{FW}_{20\%}$), a term that is analogous to $W(K_1)$ from Ayres (1979). Regression coefficients are reported in Table 4. Simplifying the linear model expressions into the original unscaled predictor variables rather than PCs, we find that for the $\text{Ly}\alpha$ emission line:

$$\log_{10} \text{FW}_{20\%} = -0.29 \log_{10} g + 0.09 \log_{10} \frac{L(\text{SiIII})}{L(\text{bol})} + 2.13 \log_{10} T_{\text{eff}} - 5.54, \quad (5)$$

where $\text{FW}_{20\%}$ is in \AA , g is in cm s^{-2} , $L(\text{SiIII})/L_{\text{bol}}$ is unitless, and T_{eff} is in K. There are some similarities in the coefficients between this paper’s Equation 5 and Equation 8 from Linsky (1980) ($\log W(K_1) = -0.25 \log g + 0.25 \log F + 1.75 \log T_{\text{eff}} + 0.25 \log A_{\text{met}}$, where F is the scaled non-radiative heating rate and A_{met} is the metal abundance), such as the sign and magnitude of each coefficient being roughly the same. Dissimilarities are likely due to the differences in terms (F and A_{met}) and parameter ranges in the sample stars. In this analysis, the stars used have $\log_{10} g$ between

Table 2. Principal Component Analysis Summary

Eigenvector (PC)	Eigenvalue	Correlation coefficients with Predictor Variables						Regression coefficients (β)	
		g		L(SiIII)/Lbol		T_{eff}		Response Variable	
		ρ	p	ρ	p	ρ	p	FW _{20%}	
PC ₁	1.55	-0.89	4.5×10^{-6}	0.75	7.6×10^{-4}	0.44	0.09	$\beta_1=0.60$	
PC ₂	1.02	-0.02	0.95	-0.53	0.04	0.86	1.8×10^{-5}	$\beta_2=0.10$	
PC ₃	0.43	-0.5	0.07	-0.4	0.13	-0.3	0.35	—	

NOTE—The principal components (PCs) are related to the scaled predictor variables as follows: $PC_1 = -0.71 \log_{10} g + 0.60 \log_{10} L(\text{SiIII})/L_{bol} + 0.36 \log_{10} T_{eff}$; $PC_2 = -0.02 \log_{10} g - 0.52 \log_{10} L(\text{SiIII})/L_{bol} + 0.85 \log_{10} T_{eff}$; $PC_3 = -0.70 \log_{10} g - 0.60 \log_{10} L(\text{SiIII})/L_{bol} - 0.38 \log_{10} T_{eff}$. ρ is the correlation coefficient and p is the probability of no correlation between the PCs and predictor variables. We define a significant correlation as $|\rho| > 0.5$; $p < 0.05$. The regression coefficients relate the PCs and response variable as follows: $\log_{10} \text{FW}_{20\%} = PC_1 \times \beta_1 + PC_2 \times \beta_2$. The intercept coefficient on the regression is vanishingly small ($< 10^{-15}$) and is dropped. The linear model’s predicted $\text{FW}_{20\%}$ is significantly and positively correlated with the measured values ($\rho=0.76$, $p=6.5 \times 10^{-4}$).

3.9-5.2, $\log_{10} L(\text{SiIII})/L_{bol}$ between -7.5 and -5.0, and T_{eff} between 3000-3900 K. The observed range of $\text{FW}_{20\%}$ values is 0.6-3.8 Å.

As is the case for Ca II, stellar activity appears to be a minor factor in the width of $\text{Ly}\alpha$, also indicated by the lack of correlation between $\text{FW}_{20\%}$ and $L(\text{Ly}\alpha)/L_{bol}$ ($\rho=-0.06$, $p=0.82$) or $L(\text{SiIII})/L_{bol}$ ($\rho=0.29$, $p=0.27$). The more dominant factors are surface gravity and effective temperature, indicated by the correlation coefficients between $\text{FW}_{20\%}$ and T_{eff} ($\rho=0.50$; $p=0.05$) or g ($\rho=-0.51$; $p=0.04$). From Figure 3, we find that in general, the M dwarfs with larger $\text{Ly}\alpha$ wing flux values tend to be more active. The “inactive” MUSCLES M dwarfs (as determined by optical activity indicators such as Ca II; France et al. 2016) have the narrowest profiles, and Proxima Centauri has a surprisingly narrow profile given its known levels of moderate activity (Robertson et al. 2013, 2016; Davenport et al. 2016; Howard et al. 2018). For example, Proxima Centauri’s $\log_{10} L(\text{SiIII})/L_{bol} = -6.2$ compared to the -7.2 to -7.5 values for the inactive MUSCLES M dwarfs GJ 832, GJ 581, and GJ 436. However, as discussed, these line widths are dominated by stellar structure, and in general, lower surface gravity (i.e., young) M dwarfs tend to be more active.

4.2. Chromospheric electron density estimates from $\text{Ly}\alpha$ observations

The electron density in the line forming region (the chromosphere for the $\text{Ly}\alpha$ broad wings) is a main factor in controlling the width of the $\text{Ly}\alpha$ line (Gayley 1994). We estimate chromosphere electron density values, which are a valuable constraint for stellar models, using the formalism from Gayley (1994) that explicitly relates the surface flux density of the $\text{Ly}\alpha$ broad wings to chromospheric electron density and other stellar properties:

$$F_{wing}(\Delta\lambda) \approx \frac{F_{peak,\odot}}{\Delta\lambda^2} \left(\frac{n_e}{n_{e,\odot}} \right)^2 \frac{g_\odot}{g} \frac{T_{chromo}}{7500K} \frac{J_{2c,\odot}}{J_{2c}}, \quad (6)$$

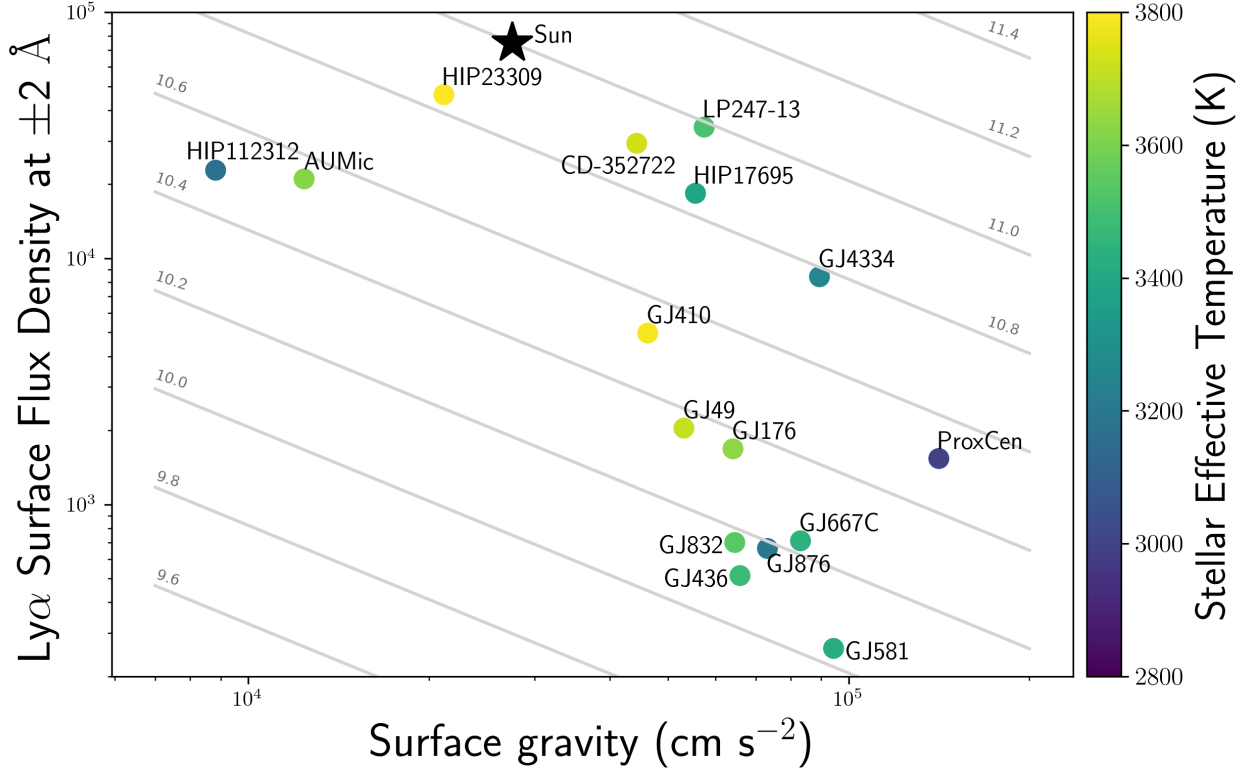


Figure 5. Surface gravity vs. surface flux density ($\text{erg cm}^{-2} \text{s}^{-1} \text{\AA}^{-1}$) at $\pm 2 \text{\AA}$ from $\text{Ly}\alpha$ line center. Lines of constant electron density ($\log_{10} n_e$) are shown in gray under the approximation from Gayley (1994) (Equation 6, with $T_{\text{chromo}} = 7500 \text{ K}$, and $J_{2c} = J_{2c,\odot}$). Note that the Sun’s measured electron density is 10^{11} cm^{-3} (Song 2017) and GJ 832’s is 10^{10} cm^{-3} (Fontenla et al. 2016).

where $F_{\text{wing}}(\Delta\lambda)$ is the $\text{Ly}\alpha$ surface flux density at $\Delta\lambda \text{\AA}$ from line center, $F_{\text{peak},\odot}$ is the peak solar $\text{Ly}\alpha$ flux ($\sim 3 \times 10^5 \text{ erg cm}^{-2} \text{s}^{-1}$), n_e is the chromospheric electron density, g is the surface gravity, T_{chromo} is the chromospheric temperature, and J_{2c} is the Balmer continuum flux. Each parameter is normalized to the solar (\odot) value. Stars with larger electron densities and hotter chromospheres will have broader wings, but the wing intensity is diminished for stars with greater surface gravity and greater Balmer continuum flux.

Figure 5 shows the $\text{Ly}\alpha$ surface flux densities of the FUMES targets, the MUSCLES M dwarfs (France et al. 2016), Proxima Centauri and AU Mic (Youngblood et al. 2017), and the Sun (SORCE/SOLSTICE; McClintock et al. 2005), plotted against surface gravity. Lines of constant electron density are drawn on the plot using Equation 6. We assume T_{chromo} and J_{2c} are both equivalent to solar values ($T_{\text{chromo}} = 7500 \text{ K}$; $J_{2c} = 1.7 \times 10^5 \text{ erg cm}^{-2} \text{s}^{-1} \text{\AA}^{-1} \text{sr}^{-1}$). For stars with known chromospheric electron densities, the Gayley (1994) approximation works well. The Sun’s electron density $\log_{10} n_e = 11 \text{ cm}^{-3}$ (Song 2017), and GJ 832’s $\log_{10} n_e = 10 \text{ cm}^{-3}$ (Fontenla et al. 2016), are both in agreement with the gray curves in Figure 5.

We find that LP 247-13, a 625 Myr M2.7V star, has a chromospheric electron density similar to the Sun. All of the FUMES targets (“active” stars) have electron densities larger than that of the “inactive” M dwarfs from the MUSCLES survey, except for GJ 176. We note that GJ 176 is the least “inactive” of the MUSCLES stars as it is the most rapidly rotating ($P_{\text{rot}}=39.5$ day, Robertson et al. 2015) and is possibly younger than 1 Gyr based on its large X-ray luminosity (Guinan et al. 2016; Loyd et al. 2018).

4.3. STIS G140L and future Ly α observations

The presented Ly α reconstructions are the first based on $\lambda/\Delta\lambda \sim 1,000$ spectra with the ISM H I absorption completely unresolved. Using the STIS G140L mode provides some observational advantages including avoiding prohibitively long exposure times of higher resolution STIS modes for M dwarf targets deemed too hazardous for the COS instrument (Bright Object Protections⁸). Based on the six M dwarfs presented here, we find that the precision of Ly α reconstructions performed on STIS G140L spectra can range from 5% to 100% at the 68% confidence level (Figure 6). At the 95% confidence level, the precisions range from $\sim 10\%$ to a factor of nine. There appears to be no dependence of these precisions on the SNR of the observed spectrum; we note that all G140L Ly α emission lines were detected at high SNR (90-250 integrated over the line). Rather, our three G140L targets with the largest reconstructed flux uncertainties (GJ 4334, GJ 49, and GJ 410) are also the G140L targets with the lowest surface flux in the Ly α wings, or in other words, the narrowest profiles. We hypothesize that for narrow profiles (Ly α surface flux at $\pm 2 \text{ \AA} \lesssim 10^4 \text{ erg cm}^{-2} \text{ s}^{-1} \text{ \AA}$ or $FW_{20\%} < 2.5\text{-}3.0 \text{ \AA}$), the spectrum does not provide enough spectrally-resolved information for the fit to distinguish between large flux, large ISM column solutions and small flux, small ISM column solutions. The higher resolution E140M grating results in reconstructed flux precisions of approximately 2-4% at the 68% confidence level for high SNRs (we note that the two stars with E140M observations, HIP 112312 and HIP 17695, have a line-integrated SNR = 70-90). However, for lower SNR spectra, Youngblood et al. (2016) found uncertainties up to 150% in E140M reconstructions of K dwarfs (HD 97658, HD 40307, HD 85512) with SNR = 20-30 integrated over the line. The precision found by Youngblood et al. (2016) with the STIS G140M grating ($\lambda/\Delta\lambda \sim 10,000$) is 5-30% for medium-to-high SNRs and can be a factor of ~ 2 for low SNRs (e.g., GJ 1214, SNR=4 integrated over the line). Thus, STIS G140L spectra can produce reconstructed Ly α fluxes for young, active M dwarfs with precisions comparable to G140M spectra, but the precision is much lower than what is obtainable with high SNR G140M or E140M spectra.

Adopting $FW_{20\%} > 2.5 \text{ \AA}$ as the threshold between precise and imprecise Ly α reconstructions with G140L, Equation 5 may be useful for guiding future observers toward whether or not G140L is suitable for a Ly α reconstruction for a particular M dwarf. Surface gravity and effective temperature, two of the three stellar parameters in Equation 5, are readily available in the literature for many M dwarfs. The third parameter, $L(\text{SiIII})/L(\text{bol})$, is not available for most M dwarfs, but can be estimated from the stellar rotation period (Pineda et al. *accepted*) or common activity indicators like R'_{HK} or $L(\text{H}\alpha)/L(\text{bol})$ (Melbourne et al. 2020).

Figure 6 shows how the observed Ly α fluxes compare to the reconstructed (intrinsic) fluxes. The observed fluxes were obtained simply by integrating over the observed, ISM-attenuated Ly α profiles. In some cases, the observed Ly α fluxes are only 10-50% less than the reconstructed fluxes, while in

⁸ http://www.stsci.edu/hst/cos/documents/isrs/ISR2017_01.pdf

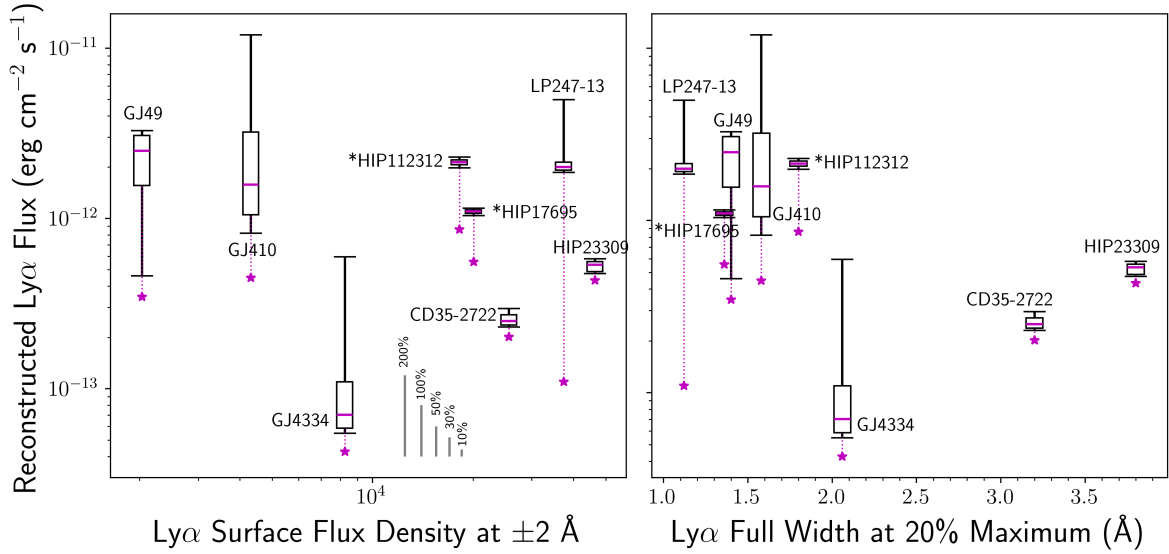


Figure 6. The reconstructed $\text{Ly}\alpha$ flux as observed at Earth are plotted against the $\text{Ly}\alpha$ surface flux density ($\text{erg cm}^{-2} \text{s}^{-1} \text{\AA}^{-1}$ at $\pm 2 \text{\AA}$ from line center (*left panel*) and $\text{Ly}\alpha$ full width at 20% maximum ($FW_{20\%}$; *right panel*) for the FUMES targets. All but two stars were observed with the STIS G140L grating ($\lambda/\Delta\lambda \sim 1,000$); HIP 112312 and HIP 17695 were observed with the STIS E140M grating ($\lambda/\Delta\lambda \sim 45,000$) and are labeled with asterisks. The magenta horizontal line in each white box represents the median flux, the white boxes represent the 68% confidence interval, and the black error bars represent the 95% confidence interval. The small magenta stars show the $\text{Ly}\alpha$ flux density obtained by integrating over the observed (ISM-attenuated) $\text{Ly}\alpha$ spectra. The gray vertical lines indicate the apparent size of several factors of uncertainty (200%, 100%, 50%, 30%, and 10%).

others they are a factor of a few to an order of magnitude less. The dominant factor in the flux differences is the column density of the ISM absorbers and the radial velocity of the ISM absorbers relative to the stellar radial velocity. A small radial velocity offset between the star and ISM, and larger column densities will result in larger flux differences between observed and reconstructed. Figure 6 may give the reader a sense of whether or not performing a reconstruction on G140L $\text{Ly}\alpha$ spectra is worthwhile for their science goals.

5. SUMMARY

As part of the Far Ultraviolet M-dwarf Evolution Survey (FUMES), we have reconstructed the intrinsic $\text{Ly}\alpha$ profiles of 8 early-to-mid M dwarfs spanning a range of young to field star ages from low and moderate resolution spectra taken with *HST*'s STIS spectrograph. The $\text{Ly}\alpha$ and Si III fluxes derived in this paper are incorporated into Paper I of the FUMES survey (Pineda et al. *accepted*), which describes the flux evolution of FUV spectral lines with stellar age and rotation period for early-to-mid M dwarfs. We summarize our findings here:

1. We present the first demonstration of $\text{Ly}\alpha$ reconstruction on low, $\lambda/\Delta\lambda \sim 1,000$ resolution spectra, where the H I absorption trough from the ISM is completely unresolved. We find that

the $1\text{-}\sigma$ precision in the reconstructed $\text{Ly}\alpha$ flux can be 5-10% in the best case (young M dwarfs) and a factor of two in the worst case (field age M dwarfs). The precision is not correlated with SNR of the observation, rather, it depends on the intrinsic broadness of the stellar $\text{Ly}\alpha$ line. Young, low-gravity stars have the broadest lines and therefore provide more information at low spectral resolution to the fit to break degeneracies among model parameters.

2. Our high SNR, low resolution $\text{Ly}\alpha$ spectra detect the extremely broad wings ($\sim 500\text{-}1000\text{ km s}^{-1}$) at SNR=7-14 per resolution element, and we see large differences in the width of $\text{Ly}\alpha$ from star to star. We confirm past findings that the line width is predominantly correlated with the fundamental stellar parameters surface gravity and effective temperature, rather than magnetic activity.
3. $\text{Ly}\alpha$ surface flux density $\sim 2\text{ \AA}$ from line center may predict electron density values in the chromosphere, as shown by Gayley (1994). We confirm the validity of the $\text{Ly}\alpha$ surface flux density approximation from that work using GJ 832's spectrum from Youngblood et al. (2016); Loyd et al. (2016) and modeled electron density from Fontenla et al. (2016).

The data presented here were obtained as part of the *HST* Guest Observing program #14640. A.Y. acknowledges support by an appointment to the NASA Postdoctoral Program at Goddard Space Flight Center, administered by USRA through a contract with NASA. We thank J. Linsky, T. Barclay, and A. Wolfgang for helpful discussions, and E. R. Newton and W. C. Waalkes for their contributions to lyapy.

Facilities: HST

Software: Astropy (Robitaille et al. 2013), IPython (Perez & Granger 2007), Matplotlib (Hunter 2007), NumPy and SciPy (vander Walt et al. 2011), lyapy (Youngblood et al. 2016), emcee (Foreman-Mackey et al. 2013), triangle (Foreman-Mackey et al. 2014), statsmodels (Seabold & Perktold 2010).

REFERENCES

- Ayres, T. R. 1979, *The Astrophysical Journal*, 228, 509, doi: [10.1086/156873](https://doi.org/10.1086/156873)
- Ayres, T. R. 2010, *ApJS*, 187, 149, doi: [10.1088/0067-0049/187/1/149](https://doi.org/10.1088/0067-0049/187/1/149)
- Basri, G. S., Linsky, J. L., Bartoe, J.-D. F., Brueckner, G., & van Hoosier, M. E. 1979, *The Astrophysical Journal*, 230, 924, doi: [10.1086/157151](https://doi.org/10.1086/157151)
- Bell, C. P. M., Mamajek, E. E., & Naylor, T. 2015, *MNRAS*, 454, 593, doi: [10.1093/mnras/stv1981](https://doi.org/10.1093/mnras/stv1981)
- Bourrier, V., Ehrenreich, D., Allart, R., et al. 2017, *A&A*, 602, A106, doi: [10.1051/0004-6361/201730542](https://doi.org/10.1051/0004-6361/201730542)
- Brown, A. G. A., Vallenari, A., Prusti, T., et al. 2018, *Astronomy & Astrophysics*, 616, A1, doi: [10.1051/0004-6361/201833051](https://doi.org/10.1051/0004-6361/201833051)
- Cassatella, A., Altamore, A., Badiali, M., & Cardini, D. 2001, *Astronomy and Astrophysics*, 374, 1085, doi: [10.1051/0004-6361:20010816](https://doi.org/10.1051/0004-6361:20010816)
- Curdtt, W., Brekke, P., Feldman, U., et al. 2001, *A&A*, 375, 591, doi: [10.1051/0004-6361:20010364](https://doi.org/10.1051/0004-6361:20010364)
- Davenport, J. R. A., Kipping, D. M., Sasselov, D., Matthews, J. M., & Cameron, C. 2016, *ApJL*, 829, L31, doi: [10.3847/2041-8205/829/2/L31](https://doi.org/10.3847/2041-8205/829/2/L31)
- Donati, J.-F., Morin, J., Petit, P., et al. 2008, *Monthly Notices of the Royal Astronomical Society*, 390, 545, doi: [10.1111/j.1365-2966.2008.13799.x](https://doi.org/10.1111/j.1365-2966.2008.13799.x)
- dos Santos, L. A., Ehrenreich, D., Bourrier, V., et al. 2019, *A&A*, 629, A47, doi: [10.1051/0004-6361/201935663](https://doi.org/10.1051/0004-6361/201935663)

Table 3. Prior Probabilities, Best Fits, and Confidence Intervals for G140L

Parameter	GJ 4334	GJ 49
V_{radial} (km s ⁻¹)	U(-100; 300) [142.4, 153.0, 166.7, 178.0, 188.9]	U(-150; 150) [43.8, 50.9, 52.8, 54.0, 55.1]
$\log_{10} A$ (erg cm ⁻² s ⁻¹ Å ⁻¹)	U(-18.5, 8) [-12.99, -12.89, -12.72, -12.36, -10.95]	U(-14; -10) [-11.93, -11.07, -10.52, -10.32, -10.26]
$FWHM_L$ (km s ⁻¹)	U(1; 1000) [8.6, 37.9, 57.5, 73.6, 88.1]	U(1; 1000) [9.3, 10.1, 12.6, 23.7, 62.3]
$FWHM_G$ (km s ⁻¹)	U(1; 1000) [167.4, 209.5, 253.7, 293.4, 327.1]	U(1; 1000) [178.8, 181.8, 187.7, 208.4, 277.2]
$\log_{10} N(\text{H I})$ (cm ⁻²)	U(17.8; 19) [17.81, 17.87, 18.03, 18.25, 18.58]	U(17.7; 18.5) [17.81, 18.29, 18.44, 18.49, 18.50]
b_{HI} (km s ⁻¹)	11.5	11.5
V_{HI} (km s ⁻¹)	U(0; 300) [188.9, 214.7, 223.1, 227.8, 233.4]	U(0; 150) [47.0, 72.4, 72.8, 73.1, 73.3]
V_{SiIII}	U(-60; 400) [195.5, 221.6, 247.7, 270.6, 292.7]	U(-250; 250) [76.2, 90.0, 104.2, 118.7, 132.9]
A_{SiIII}	U(-16; -12) [-14.94, -14.85, -14.75, -14.61, -14.37]	U(-16; -13) [-14.55, -14.49, -14.44, -14.37, -14.30]
$FWHM_{SiIII}$	U(1; 700) [130.1, 202.1, 277.0, 344.4, 416.7]	U(1; 700) [253.0, 300.1, 349.5, 400.6, 453.1]
$F(\text{Ly}\alpha)$ (erg cm ⁻² s ⁻¹)	[5.47, 5.87, 7.03, 10.96, 59.54] $\times 10^{-14}$	[0.46, 1.56, 2.49, 3.07, 3.28] $\times 10^{-12}$
$F(\text{Si III})$ (erg cm ⁻² s ⁻¹)	[1.78, 1.93, 2.11, 2.28, 2.44] $\times 10^{-15}$	[5.06, 5.27, 5.50, 5.71, 5.90] $\times 10^{-15}$

NOTE—U represents a uniform prior within the bounds. Other values are fixed values. On the second line: [2.5%, 15.9%, 50%, 84.1%, 97.5%].

Dring, A. R., Linsky, J., Murthy, J., et al. 1997, The Astrophysical Journal, 488, 760
 Durbin, J., & Watson, G. S. 1950, Biometrika, 37, 409, doi: [10.1093/biomet/37.3-4.409](https://doi.org/10.1093/biomet/37.3-4.409)
 Fontenla, J., Witbrod, J., Linsky, J. L., et al. 2016, The Astrophysical Journal, 830, 154
 Foreman-Mackey, D., Hogg, D. W., Lang, D., & Goodman, J. 2013, Publications of the Astronomical Society of the Pacific, 125, 306, doi: [10.1086/670067](https://doi.org/10.1086/670067)
 Foreman-Mackey, D., Ryan, G., Barbary, K., et al. 2014, doi: [10.5281/zenodo.11020](https://doi.org/10.5281/zenodo.11020)

France, K., Froning, C. S., Linsky, J. L., et al. 2013, The Astrophysical Journal, 763, 149, doi: [10.1088/0004-637X/763/2/149](https://doi.org/10.1088/0004-637X/763/2/149)
 France, K., Loyd, R., Youngblood, A., et al. 2016, Astrophysical Journal, 820, doi: [10.3847/0004-637X/820/2/89](https://doi.org/10.3847/0004-637X/820/2/89)
 Gagné, J., & Faherty, J. K. 2018, ApJ, 862, 138, doi: [10.3847/1538-4357/aaca2e](https://doi.org/10.3847/1538-4357/aaca2e)
 Gayley, K. G. 1994, The Astrophysical Journal, 431, 806, doi: [10.1086/174531](https://doi.org/10.1086/174531)
 Guinan, E. F., Engle, S. G., & Durbin, A. 2016, ApJ, 821, 81, doi: [10.3847/0004-637X/821/2/81](https://doi.org/10.3847/0004-637X/821/2/81)

Table 4. Prior Probabilities, Best Fits, and Confidence Intervals for G140L

Parameter	GJ 410	LP247-13
V_{radial} (km s ⁻¹)	U(-250; 250) [0.8, 8.7, 16.8, 25.5, 36.8]	U(-250; 250) [84.8, 91.6, 101.3, 110.2, 115.3]
$\log_{10} A$ (erg cm ⁻² s ⁻¹ Å ⁻¹)	U(-18.5; -8) [-11.6, -11.38, -11.04, -10.44, -9.3]	U(-18; -8) [-12.27, -12.19, -12.0, -11.58, -11.04]
FWHM_L (km s ⁻¹)	U(1; 1000) [3.8, 13.8, 27.3, 40.2, 51.6]	U(1; 1000) [22.6, 41.6, 66.7, 82.7, 91.4]
FWHM_G (km s ⁻¹)	U(1; 1000) [158.4, 181.8, 204.7, 226.6, 246.6]	U(1; 1000) [17.5, 72.2, 118.1, 153.6, 178.3]
$\log_{10} N(\text{H I})$ (cm ⁻²)	U(17.5; 19) [18.05, 18.18, 18.32, 18.48, 18.68]	U(18.3; 19) [18.3, 18.31, 18.35, 18.42, 18.50]
b_{HI} (km s ⁻¹)	11.5	11.5
V_{HI} (km s ⁻¹)	U(-200; 200) [71.4, 72.7, 73.6, 74.7, 76.0]	U(-250; 250) [74.4, 76.0, 78.8, 84.4, 88.4]
V_{SiIII} (km s ⁻¹)	U(-160; 350) [-33.7, -11.8, 9.8, 31.6, 53.6]	U(-250; 250) [121.1, 143.8, 166.6, 188.7, 209.8]
A_{SiIII} (erg cm ⁻² s ⁻¹ Å ⁻¹)	U(-16; -12) [-14.28, -14.19, -14.1, -13.99, -13.75]	U(-16; -13) [-14.50, -14.43, -14.36, -14.28, -14.20]
$\text{FWHM}_{\text{SiIII}}$ (km s ⁻¹)	U(1; 700) [113.1, 197.5, 257.5, 313.7, 374.1]	U(1; 700) [268.3, 325.2, 391.3, 464.7, 539.7]
$F(\text{Ly}\alpha)$ (erg cm ⁻² s ⁻¹)	[0.82, 1.05, 1.58, 3.21, 11.95] $\times 10^{-12}$	[3.06, 3.39, 4.42, 8.16, 17.17] $\times 10^{-12}$
$F(\text{Si III})$ (erg cm ⁻² s ⁻¹)	[7.32, 8.02, 8.76, 9.48, 10.16] $\times 10^{-15}$	[6.53, 6.91, 7.31, 7.72, 8.10] $\times 10^{-15}$

NOTE—U represents a uniform prior within the bounds. Other values are fixed values. On the second line: [2.5%, 15.9%, 50%, 84.1%, 97.5%].

Hartman, J. D., Bakos, G. Á., Noyes, R. W., et al. 2011, *The Astronomical Journal*, 141, 166, doi: [10.1088/0004-6256/141/5/166](https://doi.org/10.1088/0004-6256/141/5/166)
Howard, W. S., Tilley, M. A., Corbett, H., et al. 2018, *ApJL*, 860, L30, doi: [10.3847/2041-8213/aacaf3](https://doi.org/10.3847/2041-8213/aacaf3)
Hunter, J. D. 2007, *Computing in Science & Engineering*, 9, 90, doi: [10.1109/MCSE.2007.55](https://doi.org/10.1109/MCSE.2007.55)
Irwin, J., Berta, Z. K., Burke, C. J., et al. 2011, *ApJ*, 727, 56, doi: [10.1088/0004-637X/727/1/56](https://doi.org/10.1088/0004-637X/727/1/56)
Linsky, J. L. 1980, *Annual Review of Astronomy and Astrophysics*, 18, 439, doi: [10.1146/annurev.aa.18.090180.002255](https://doi.org/10.1146/annurev.aa.18.090180.002255)

Linsky, J. L., Draine, B. T., Moos, H. W., et al. 2006, *The Astrophysical Journal*, 647, 1106, doi: [10.1086/505556](https://doi.org/10.1086/505556)
Lloyd, R. O. P., France, K., Youngblood, A., et al. 2016, *The Astrophysical Journal*, 824, 102, doi: [10.3847/0004-637X/824/2/102](https://doi.org/10.3847/0004-637X/824/2/102)
—. 2018, *The Astrophysical Journal*, 867, 71, doi: [10.3847/1538-4357/aae2bd](https://doi.org/10.3847/1538-4357/aae2bd)
McClintock, W., Linsky, J. L., Henry, R. C., & Moos, H. W. 1975, *The Astrophysical Journal*, 202, 733, doi: [10.1086/154026](https://doi.org/10.1086/154026)

Table 5. Prior Probabilities, Best Fits, and Confidence Intervals for G140L (continuation of Table 3)

Parameter	CD 35-2722	HIP 23309
V_{radial} (km s ⁻¹)	U(-250; 250) [70.3, 93.3, 99.1, 104.7, 110.1]	U(-250; 250) [110.4, 114.5, 118.0, 121.6, 125.1]
$\log_{10} A$ (erg cm ⁻² s ⁻¹ Å ⁻¹)	U(-18, -8) [-12.79, -12.75, -12.70, -12.63, -12.51]	U(-18; -8) [-12.26, -12.23, -12.20, -12.17, -12.14]
$FWHM_L$ (km s ⁻¹)	U(1; 1000) [162.3, 186.2, 201.5, 215.3, 227.9]	U(1; 1000) [122.8, 129.0, 135.6, 142.5, 149.7]
$FWHM_G$ (km s ⁻¹)	U(1; 1000) [236.6, 294.7, 327.9, 359.9, 387.3]	U(1; 5000) [421.6, 438.7, 455.3, 472.5, 489.6]
$\log_{10} N(\text{H I})$ (cm ⁻²)	U(17.5; 19) [17.52, 17.60, 17.78, 17.98, 18.21]	U(17.5; 19) [17.61, 17.71, 17.80, 17.88, 17.96]
b_{HI} (km s ⁻¹)	11.5	11.5
V_{HI} (km s ⁻¹)	U(-250; 250) [-66.2, -58.3, 38.2, 59.0, 67.9]	U(-250; 250) [47.5, 72.0, 74.7, 76.7, 78.8]
V_{SiIII}	U(-250; 250) [-7.5, 8.7, 25.1, 42.1, 67.9]	U(-250; 250) [96.3, 107.5, 118.1, 128.5, 138.6]
A_{SiIII}	U(-16; -13) [-14.28, -14.23, -14.17, -14.11, -14.03]	U(-16; -13) [-13.86, -13.82, -13.77, -13.72, -13.64]
$FWHM_{SiIII}$	U(1; 700) [338.8, 409.7, 477.8, 548.6, 616.4]	U(1; 700) [201.1, 243.0, 276.1, 306.9, 336.5]
$F(\text{Ly}\alpha)$ (erg cm ⁻² s ⁻¹)	[2.30, 2.37, 2.50, 2.72, 2.99] $\times 10^{-13}$	[5.03, 5.21, 5.40, 5.60, 5.82] $\times 10^{-13}$
$F(\text{Si III})$ (erg cm ⁻² s ⁻¹)	[1.26, 1.32, 1.37, 1.43, 1.49] $\times 10^{-14}$	[1.85, 1.93, 2.01, 2.10, 2.17] $\times 10^{-14}$

NOTE—U represents a uniform prior within the bounds. Other values are fixed values. On the second line: [2.5%, 15.9%, 50%, 84.1%, 97.5%].

McClintock, W. E., Rottman, G. J., & Woods, T. N. 2005, *Solar Physics*, 230, 225, doi: [10.1007/s11207-005-7432-x](https://doi.org/10.1007/s11207-005-7432-x)

McLean, A. B., Mitchell, C. E. J., & Swanston, D. M. 1994, *Journal of Electron Spectroscopy and Related Phenomena*, 69, 125, doi: [10.1016/0368-2048\(94\)02189-7](https://doi.org/10.1016/0368-2048(94)02189-7)

Meadows, V. S., Reinhard, C. T., Arney, G. N., et al. 2018, *Astrobiology*, 18, 630, doi: [10.1089/ast.2017.1727](https://doi.org/10.1089/ast.2017.1727)

Melbourne, K., Youngblood, A., France, K., et al. 2020, *AJ*, 160, 269, doi: [10.3847/1538-3881/abbf5c](https://doi.org/10.3847/1538-3881/abbf5c)

Messina, S., Desidera, S., Turatto, M., Lanzafame, A. C., & Guinan, E. F. 2010, *A&A*, 520, A15, doi: [10.1051/0004-6361/200913644](https://doi.org/10.1051/0004-6361/200913644)

Miles, B. E., & Shkolnik, E. L. 2017, *AJ*, 154, 67, doi: [10.3847/1538-3881/aa71ab](https://doi.org/10.3847/1538-3881/aa71ab)

Milkey, R. W., & Mihalas, D. 1973, *The Astrophysical Journal*, 185, 709, doi: [10.1086/152448](https://doi.org/10.1086/152448)

Table 6. Prior Probabilities, Best Fits, and Confidence Intervals for HIP 112312 (E140M)

Parameter	Native Resolution	Degraded (G140L) Resolution
V_{radial} (km s ⁻¹)	U(-250; 250) [-3.2, -2.2, -1.1, 0.0, 1.1]	U(-100; 100) [16.1, 23.2, 31.6, 39.3, 46.1]
$\log_{10} A$ (erg cm ⁻² s ⁻¹ Å ⁻¹)	U(-18; -8) [-11.15, -11.13, -11.10, -11.07, -11.04]	U(-18; -8) [-11.89, -11.82, -11.70, -11.44, -10.81]
$FWHM_L$ (km s ⁻¹)	U(1; 1000) [37.8, 40.1, 42.6, 45.1, 47.5]	U(1; 1000) [44.9, 90.9, 122.9, 143.8, 158.1]
$FWHM_G$ (km s ⁻¹)	U(1; 1000) [216.3, 221.3, 226.4, 231.6, 236.5]	U(1; 1000) [4.4, 22.5, 71.5, 127.8, 165.3]
$\log_{10} N(\text{H I})$ (cm ⁻²)	U(17.5; 19) [18.24, 18.26, 18.28, 18.3, 18.33]	U(17.5; 19.0) [17.52, 17.61, 17.82, 18.08, 18.39]
b_{HI} (km s ⁻¹)	$\ln(5; 20)$ [10.2, 11.4, 12.2, 12.7, 13.2]	$\ln(5; 20)$ [5.6, 8.3, 13.0, 17.3, 19.4]
V_{HI} (km s ⁻¹)	U(-250; 250) [-10.3, -9.9, -9.5, -9.0, -8.6]	U(-100; 100) [-27.7, -15.1, 0.7, 15.0, 23.5]
$F(\text{Ly}\alpha)$ (erg cm ⁻² s ⁻¹)	[2.02, 2.08, 2.14, 2.21, 2.29] $\times 10^{-12}$	[1.22, 1.31, 1.48, 1.90, 3.17] $\times 10^{-12}$

NOTE—U represents a uniform prior within the bounds. Other values are fixed values. On the second line: [2.5%, 15.9%, 50%, 84.1%, 97.5%].

- Morton, D. C., & Widing, K. G. 1961, The Astrophysical Journal, 133, 596, doi: [10.1086/147062](https://doi.org/10.1086/147062)
- Newton, E. R., Charbonneau, D., Irwin, J., et al. 2014, The Astronomical Journal, 147, 20, doi: [10.1088/0004-6256/147/1/20](https://doi.org/10.1088/0004-6256/147/1/20)
- Newton, E. R., Irwin, J., Charbonneau, D., Berta-Thompson, Z. K., & Dittmann, J. A. 2016, The Astrophysical Journal, 821, L19, doi: [10.3847/2041-8205/821/1/L19](https://doi.org/10.3847/2041-8205/821/1/L19)
- Pagano, I., Linsky, J. L., Carkner, L., et al. 2000, ApJ, 532, 497, doi: [10.1086/308559](https://doi.org/10.1086/308559)
- Peacock, S., Barman, T., Shkolnik, E. L., Hauschildt, P. H., & Baron, E. 2019a, The Astrophysical Journal, 871, 235, doi: [10.3847/1538-4357/aaf891](https://doi.org/10.3847/1538-4357/aaf891)
- Peacock, S., Barman, T., Shkolnik, E. L., et al. 2019b, The Astrophysical Journal, 886, 77, doi: [10.3847/1538-4357/ab4f6f](https://doi.org/10.3847/1538-4357/ab4f6f)
- Perez, F., & Granger, B. E. 2007, Computing in Science & Engineering, 9, 21, doi: [10.1109/MCSE.2007.53](https://doi.org/10.1109/MCSE.2007.53)
- Redfield, S., & Linsky, J. L. 2000, The Astrophysical Journal, 534, 825, doi: [10.1086/308769](https://doi.org/10.1086/308769)
- Redfield, S., & Linsky, J. L. 2004, ApJ, 602, 776, doi: [10.1086/381083](https://doi.org/10.1086/381083)
- Redfield, S., & Linsky, J. L. 2008, The Astrophysical Journal, 673, 283, doi: [10.1086/524002](https://doi.org/10.1086/524002)
- Robertson, P., Bender, C., Mahadevan, S., Roy, A., & Ramsey, L. W. 2016, ApJ, 832, 112, doi: [10.3847/0004-637X/832/2/112](https://doi.org/10.3847/0004-637X/832/2/112)
- Robertson, P., Endl, M., Cochran, W. D., & Dodson-Robinson, S. E. 2013, ApJ, 764, 3, doi: [10.1088/0004-637X/764/1/3](https://doi.org/10.1088/0004-637X/764/1/3)
- Robertson, P., Roy, A., & Mahadevan, S. 2015, The Astrophysical Journal, 805, L22, doi: [10.1088/2041-8205/805/2/L22](https://doi.org/10.1088/2041-8205/805/2/L22)
- Robitaille, T. P., Tollerud, E. J., Greenfield, P., et al. 2013, Astronomy & Astrophysics, 558, A33, doi: [10.1051/0004-6361/201322068](https://doi.org/10.1051/0004-6361/201322068)

Table 7. Prior Probabilities, Best Fits, and Confidence Intervals for HIP 17695 (E140M)

Parameter	Native Resolution	Degraded (G140L) Resolution
V_{radial} (km s ⁻¹)	U(-50; 50) [10.3, 11.4, 12.6, 13.8, 14.9]	U(-100; 100) [37.9, 45.5, 53.0, 58.4, 62.7]
log ₁₀ A (erg cm ⁻² s ⁻¹ Å ⁻¹)	U(-18; -8) [-11.59, -11.57, -11.54, -11.52, -11.49]	U(-18; 8) [-11.99, -11.91, -11.74, -11.35, -10.87]
FWHM _L (km s ⁻¹)	U(1; 1000) [54.7, 57.7, 60.9, 64.0, 67.2]	U(1; 1000) [36.8, 64.0, 98.9, 121.5, 137.3]
FWHM _G (km s ⁻¹)	U(1; 1000) [143.2, 149.6, 156.2, 162.9, 169.4]	U(1; 1000) [19.0, 70.8, 110.0, 151.1, 189.5]
log ₁₀ N(H I) (cm ⁻²)	U(17.8; 18.0) [17.80, 17.80, 17.81, 17.82, 17.84]	U(17.5; 19.0) [17.51, 17.55, 17.69, 17.93, 18.19]
b _{HI} (km s ⁻¹)	ln(5; 20) [11.8, 12.0, 12.2, 12.5, 12.6]	ln(5; 20) [5.3, 6.8, 10.1, 14.0, 18.0]
V _{HI} (km s ⁻¹)	U(-50; 50) [15.1, 15.5, 15.9, 16.3, 16.8]	U(-100; 100) [-7.5, 16.3, 32.1, 42.1, 51.1]
F(Lyα) (erg cm ⁻² s ⁻¹)	[1.04, 1.07, 1.10, 1.12, 1.15] ×10 ⁻¹²	[0.86, 0.93, 1.15, 1.88, 3.50] ×10 ⁻¹²

NOTE—U represents a uniform prior within the bounds. On the second line: [2.5%, 15.9%, 50%, 84.1%, 97.5%].

Schneider, A. C., Shkolnik, E. L., Barman, T. S., & Loyd, R. P. 2019, *ApJ*, 886, 19, doi: [10.3847/1538-4357/ab48de](https://doi.org/10.3847/1538-4357/ab48de)

Schwieterman, E. W., Kiang, N. Y., Parenteau, M. N., et al. 2018, *Astrobiology*, 18, 663, doi: [10.1089/ast.2017.1729](https://doi.org/10.1089/ast.2017.1729)

Seabold, S., & Perktold, J. 2010, in 9th Python in Science Conference

Segura, A., Kasting, J. F., Meadows, V., et al. 2005, *Astrobiology*, 5, 706

Shkolnik, E. L., & Barman, T. S. 2014, *AJ*, 148, 64, doi: [10.1088/0004-6256/148/4/64](https://doi.org/10.1088/0004-6256/148/4/64)

Song, P. 2017, *The Astrophysical Journal*, 846, 92, doi: [10.3847/1538-4357/aa85e1](https://doi.org/10.3847/1538-4357/aa85e1)

Terrien, R. C., Mahadevan, S., Bender, C. F., Deshpande, R., & Robertson, P. 2015. <https://arxiv.org/abs/1503.01776>

Tilipman, D., Vieytes, M., Linsky, J. L., Buccino, A. P., & France, K. 2020, arXiv e-prints, arXiv:2012.11738. <https://arxiv.org/abs/2012.11738>

van der Walt, S., Colbert, S. C., & Varoquaux, G. 2011, *Computing in Science & Engineering*, 13, 22, doi: [10.1109/MCSE.2011.37](https://doi.org/10.1109/MCSE.2011.37)

West, A. A., Weisenburger, K. L., Irwin, J., et al. 2015, *The Astrophysical Journal*, 812, 3

Wilson, O. C., & Bappu, M. K. V. 1957, *The Astrophysical Journal*, 125, 661, doi: [10.1086/146339](https://doi.org/10.1086/146339)

Wood, B. E., Linsky, J. L., Hebrard, G., et al. 2004, *The Astrophysical Journal*, 609, 838, doi: [10.1086/421325](https://doi.org/10.1086/421325)

Wood, B. E., Redfield, S., Linsky, J. L., Muller, H., & Zank, G. P. 2005, *The Astrophysical Journal Supplement Series*, 159, 118, doi: [10.1086/430523](https://doi.org/10.1086/430523)

Woods, T. N., Rottman, G. J., White, O. R., Fontenla, J., & Avrett, E. H. 1995, *ApJ*, 442, 898, doi: [10.1086/175492](https://doi.org/10.1086/175492)

Youngblood, A., France, K., Loyd, R., et al. 2016, *Astrophysical Journal*, 824, doi: [10.3847/0004-637X/824/2/101](https://doi.org/10.3847/0004-637X/824/2/101)

—. 2017, *Astrophysical Journal*, 843, 31